

1 **CALIBRATING ELECTROMAGNETIC INDUCTION CONDUCTIVITIES WITH TIME-DOMAIN**

2 **REFLECTOMETRY MEASUREMENTS**

3 Dragonetti<sup>1</sup> Giovanna, Alessandro Comegna<sup>2</sup>, Ali Ajeel<sup>2</sup>, Gian Piero Deidda<sup>3</sup>, Nicola  
4 Lamaddalena<sup>1</sup>, Giuseppe Rodriguez<sup>4</sup>, Giulio Vignoli<sup>3,5</sup>, Antonio Coppola<sup>2\*</sup>

5

6 (1) Mediterranean Agronomic Institute (MAIB) - Land & Water Department, Valenzano (Bari),  
7 Italy

8 (2) University of Basilicata, School of Agricultural, Forestry and Environmental Sciences -  
9 Hydraulics and Hydrology Division, Potenza, Italy. e-mail: antonio.coppola@unibas.it

10 (3) Dipartimento di Ingegneria Civile, Ambientale e Architettura, Università di Cagliari, Cagliari,  
11 Italy

12 (4) Dipartimento di Matematica e Informatica, Università di Cagliari, Cagliari, Italy

13 (5) Groundwater and Quaternary Geology Mapping Department, Geological Survey of Denmark  
14 and Greenland, Aarhus, Denmark

15

16 **Abstract**

17 This paper deals with the issue of monitoring the spatial distribution of bulk electrical  
18 conductivity  $\sigma_b$ , in the soil root zone by using Electromagnetic Induction (EMI) sensors under  
19 different water and salinity conditions. To deduce the actual distribution of depth-specific  $\sigma_b$   
20 from EMI apparent electrical conductivity ( $EC_a$ ) measurements, we inverted the data by using a  
21 regularized 1D inversion procedure designed to manage nonlinear multiple EMI-depth  
22 responses. The inversion technique is based on the coupling of the damped Gauss-Newton  
23 method with truncated generalized singular value decomposition (TGSVD). The ill-posedness of  
24 the EMI data inversion is addressed by using a sharp stabilizer term in the objective function.

25 This specific stabilizer promotes the reconstruction of blocky targets, thereby contributing to  
26 enhance the spatial resolution of the EMI results in presence of sharp boundaries (otherwise  
27 smeared out after the application of more standard, Occam-like regularization strategies  
28 searching for smooth solutions). Time-Domain Reflectometry (TDR) data are used as ground-  
29 truth data for calibration of the inversion results. An experimental field was divided into four  
30 transects 30 m long and 2.8 m wide, cultivated with green bean and irrigated with water at two  
31 different salinity levels and using two different irrigation volumes. Clearly, this induced  
32 different salinity and water contents within the soil profiles. For each transect, 26 regularly  
33 spaced monitoring soundings (1 m apart) were selected for the collection of, respectively: (i)  
34 Geonics EM-38 and (ii) Tektronix Reflectometer data. Despite the original discrepancies in the  
35 EMI and TDR data, we found a significant correlation of the means and standard deviations of  
36 the two data series, in particular, after a low-pass spatial filtering of the TDR data. Based on  
37 these findings, the paper introduces a novel methodology to calibrate EMI-based electrical  
38 conductivities via TDR direct measurements. This calibration strategy consists in a linear  
39 mapping of the original inversion results into a new conductivity spatial distribution with the  
40 coefficients of the transformation uniquely based on the statistics of the two original  
41 measurement datasets (EMI and TDR conductivities).

42

### 43 **Introduction**

44 Soil water content and salinity vary in space both vertically and horizontally. Their distribution  
45 depends on management practices and on the complex nonlinear processes of soil water flow  
46 and solute transport, resulting in variable storages of solutes and water (Coppola et al. 2015).  
47 Monitoring the actual distribution of water and salts in the soil profile explored by roots is  
48 crucial for managing irrigation with saline water, while still maintaining an acceptable crop

49 yield. For water and salts monitoring over large areas, there are now non-invasive techniques  
50 based on electromagnetic sensors which allow the bulk electrical conductivity of soils  $\sigma_b$  to be  
51 determined (Sheets and Hendrickx 1995, Corwin and Lesch 2005, Robinson et al. 2012,  
52 Doolittle and Brevik 2014, Von Hebel et al. 2014, among many others).

53  $\sigma_b$  depends on: (i) soil water content  $\theta$ ; (ii) electrical conductivity of the soil solution (salinity)  
54  $\sigma_w$ ; (iii) tortuosity of the soil-pore system  $\tau$ ; and (iv) other factors related to the solid phase such  
55 as bulk density, clay content and mineralogy.

56 Electromagnetic induction (EMI) sensors provide measurements of the depth-weighted  
57 apparent electrical conductivity  $EC_a$  accordingly to the specific distribution of the bulk electrical  
58 conductivity  $\sigma_b$  as well as the depth response function of the sensor used (McNeill 1980). Thus,  
59 the dependence on  $\sigma_b$  makes  $EC_a$  sensitive to soil salinity and water distributions. In principle,  
60 specific procedures for estimating salinity and water content may be developed through  
61 controlled laboratory experiments where  $\sigma_b$ ,  $\sigma_w$  and  $\theta$  are measured simultaneously (Rhoades  
62 and Corwin 1981). That said, to monitor salinity and water content, it is crucial to correctly infer  
63 the depth-distribution of  $\sigma_b$  from profile-integrated  $EC_a$  readings. To date, this issue has been  
64 tackled by applying two different strategies: The first is to use empirical calibration relations  
65 relating the depth-integrated  $EC_a$  readings to the  $\sigma_b$  values measured by alternative methods -  
66 like Time-Domain Reflectometry (TDR) - within discrete depth intervals (Rhoades and Corwin  
67 1981, Lesch et al. 1992, Triantafilis, Laslett, and McBratney 2000, Amezketta 2006, Yao and Yang  
68 2010, Coppola et al. 2016); The second consists in the 1D inversion of the observations from  
69 the EMI sensor to reconstruct the vertical conductivity profile (Borchers, Uram, and Hendrickx  
70 1997, Hendrickx et al. 2002, Santos et al. 2010, Lavoué et al. 2010, Mester et al. 2011, Minsley  
71 et al. 2012, Deidda, Fenu, and Rodriguez 2014, Von Hebel et al. 2014).

72 With regard to  $EC_a$  inversion, a forward model still commonly used is the cumulative response  
73 model or local-sensitivity model (LSM) (McNeill 1980). McNeill's linear approach is well suited  
74 to the cases characterized by an induction number  $B$  (defined as the ratio between the coil  
75 distance and the skin depth) much smaller than 1. However, because of the increasing  
76 computing power, improved forward modeling algorithms based on more accurate nonlinear  
77 approaches are becoming increasingly common (Hendrickx et al. 2002, Deidda, Fenu, and  
78 Rodriguez 2014, Deidda, Bonomi, and Manzi 2003, Lavoué et al. 2010, Santos et al. 2010). For  
79 example, these more sophisticated forward modeling codes can cope with a wider range of  
80 conductivities for which the assumption  $B \ll 1$  is not necessarily met.

81 To obtain reliable vertical distributions of electrical conductivity, the  $EC_a$  data used for the  
82 inversion should consist of multi-configuration data. Hence, data collection should be  
83 performed either with the simultaneous use of different sensors or with different acquisition  
84 configurations with only one sensor (different configurations may consist, e.g., in different coil  
85 orientations, varying intercoil separations and/or frequencies – see, for example Díaz de Alba  
86 and Rodriguez, 2016). Multi-configuration data can be effectively used to invert for vertical  
87 electrical conductivity profiling since the  $EC_a$  measures actually investigate different,  
88 overlapping soil volumes. Devices specifically designed for the simultaneous acquisition of  
89 multi-configuration data are currently available. Some of them consist of one transmitter and  
90 several receivers with different coil separations and orientations (Santos et al. 2010). If,  
91 instead, a sensor with single intercoil distance and frequency is available, a possible alternative  
92 to having multi-configuration measurements could be to record the data at different heights  
93 above the ground.

94 Unfortunately, like every other physical measurement, frequency-domain electromagnetic  
95 measurements are sensitive to noise that is very hard to model effectively. Moreover as

96 discussed, for example, in Lavoué et al. (2010), Mester et al. (2011), and Von Hebel et al.  
97 (2014), an instrumental shift in conductivity values could be observed due to system  
98 miscalibration and the influence of surrounding conditions such as temperature, solar  
99 radiation, power supply conditions, the presence of the operator, zero-leveling procedures,  
100 cables close to the system and/or the field setup (see, amongst others, Sudduth, Drummond,  
101 and Kitchen 2001; Robinson et al. 2004; Abdu, Robinson, and Jones 2007; Gebbers et al. 2009;  
102 Nüsch et al. 2010). Hence, the  $EC_a$  data from EMI measurements would generally require a  
103 proper calibration. One option could be to use soil cores as ground-truth data. In this case,  $EC_a$   
104 measurements at the sampling locations can be compared against  $EC_a$  data predicted by the  
105 theoretical forward response applied to the true electrical conductivity distribution measured  
106 directly on the soil cores (Triantafyllis, Laslett, and McBratney 2000, Moghadas et al. 2012).  
107 Clearly, this strategy is extremely time- (and resource-) consuming. To avoid drilling, Lavoué et  
108 al. (2010) introduced a calibration method, later also adopted by Mester et al. (2011) and Von  
109 Hebel et al. (2014), using the electrical conductivity distribution obtained from Electrical  
110 Resistivity Tomography (ERT) data as input for electromagnetic forward modeling. The  $EC_a$   
111 values predicted on the basis of ERT data were used to remove the observed instrumental shift  
112 and correct the measured conductivity values by linear regression. However, in general, a  
113 prerequisite for such an approach concerns the reliability of the inversion of the ERT result. This  
114 is not only due to the quality of the original data, but also the adopted inversion procedure.  
115 Indeed, ERT inversion is an ill-posed problem: its solutions are characterized by non-uniqueness  
116 and instability with respect to the input data (Yu and Dougherty 2000; Zhdanov 2002; Günther  
117 2011). In the Tikhonov regularization framework, ill-posedness is addressed by including the  
118 available prior information. Such information can be very general. For example, it can be  
119 geometrical (i.e., associated to the presence of smooth or sharp boundaries between different

120 lithologies). Obviously, the final result largely reflects the initial guess formalized via the chosen  
121 regularization term (Pagliara and Vignoli 2006; Günther 2011; Vignoli, Deiana, and Cassiani  
122 2012; Fiandaca et al. 2015).

123 When relatively shallow depths have to be explored (1-2m), direct soil sampling and ERT can be  
124 effectively replaced by TDR observations. TDR devices are designed to measure the dielectric  
125 properties of soils. More precisely, they measure the apparent electrical permittivity, from  
126 which, not only the dielectric constant, but also the effective electrical conductivity can be  
127 deduced (e.g., Dalton et al. 1984; Topp et al. 1988; Weerts et al. 2001; Noborio 2001; Jones et  
128 al. 2002; Robinson et al. 2003; Lin et al. 2007; Thomsen et al. 2007; Huisman et al. 2008; Lin et  
129 al. 2008; Koestel et al. 2008; Bechtold et al. 2010). In general, TDR measurements might be  
130 difficult to be used to recover the electrical conductivity with the desired accuracy. However, in  
131 the literature, many examples are reported in which, within the range 0.002 – 0.2 S/m  
132 (compatible with the examples investigated in the present research), and by properly using the  
133 TDR device (e.g., by paying attention to minimize the effects of nonparallel device rods  
134 inserted into the ground), the TDR conductivity can be measured with an uncertainty level  
135 lower than 5% (e.g.: Huisman et al., 2008; Bechtold et al., 2010). Besides, since the TDR  
136 measurements are commonly calibrated in saline solutions just before the field data  
137 acquisitions, they could potentially provide a reliable, absolute estimation of the actual ground  
138 conductivity (Ferré et al., 1998a). For this reason, in some cases, TDR observations have been  
139 proposed as a valid tool for ground-truthing the ERT and, possibly, as ancillary information  
140 source to constraint for the ERT inversions (Koestel et al. 2008). For additional studies dealing  
141 with the use of ERT data for the validation of the EMI and TDR measurements for soil  
142 characterization we refer the reader to, for example, Cassiani et al. 2012 and Ursino et al.  
143 2014.

144 In the present research, we focus on the use of TDR data to absolute calibrate the  
145 conductivities obtained by inverting the EMI measurements. To do this, a dataset collected  
146 during an experiment carried out along four transects under different salinity and water  
147 content conditions (and monitored with both EMI and TDR sensors) is utilized. We first tackle  
148 the problem of inferring the soil electrical conductivity distribution from multi-height  $EC_a$   
149 readings via the proper inversion strategy. Then we assess the quality of these reconstructions  
150 by using TDR data as ground-truth. In this respect, in the following, we discuss how to  
151 effectively compare the  $\sigma_b$  values generated by the EMI inversion with the associated TDR  
152 values. In fact, as discussed by Coppola et al. 2016, because of their relatively smaller  
153 observation volume, TDR data provide quasi-pointlike measurements and do not integrate the  
154 small-scale variability (of soil water content, solute concentrations, etc.) induced by natural soil  
155 heterogeneity. By contrast, EMI data necessarily overrule the small-scale heterogeneities seen  
156 by TDR probes as they investigate a much larger volume. Accordingly, the paper provides a  
157 methodology to calibrate EMI results by TDR readings. This procedure lies in conditioning the  
158 original TDR data and in the statistical characteristics of the two EMI and TDR data series. On  
159 the basis of the proposed analysis, we discuss the physical reasons for the differences between  
160 EMI and TDR-based bulk electrical conductivity and identify a method to effectively migrate the  
161 reliable TDR information across the larger volume investigated by EMI.

162

### 163 **Materials and Methods**

164 The experiment was carried out at the Mediterranean Agronomic Institute of Bari (MAIB) in  
165 south-eastern Italy. The soil was pedologically classified as Colluvic Regosol, consisting of a  
166 silty-loam layer of an average depth of 0.6 m on fractured calcarenite bedrock. The  
167 experimental set-up (Fig. 1) consisted of four transects of 30 m length and 2.8 m width,

168 equipped with a drip irrigation system with five dripper lines placed 0.35 m apart and  
169 characterized by an inter-dripper distance of 0.2 m. The dripper discharge was 2 l/h. Green  
170 beans were grown in each transect. The irrigation volumes were calculated according to the  
171 time-dynamics of water content in the first 0.25 m measured by a TDR probe inserted vertically  
172 at the soil surface. TDR readings were taken: (i) just before and (ii) two hours after every  
173 irrigation. Based on the difference between the water content at field capacity and that  
174 measured just before irrigation, it was easy to assess the volumes needed to bring the soil  
175 water content back to the field capacity.

176 The four transects were irrigated with water at two different salinity levels and with two  
177 different water volumes. Transect 1: 100% of the irrigation water at 1 dSm<sup>-1</sup> (hereafter 100-  
178 1dS); Transect 2: 50% of irrigation water at 1 dSm<sup>-1</sup> (50-1dS); Transect 3: 100% of the irrigation  
179 water at 6 dSm<sup>-1</sup> (100-6dS); Transect 4: 50% of irrigation water at 6 dSm<sup>-1</sup> (50-6dS). Water  
180 salinity was induced by adding calcium chloride (CaCl<sub>2</sub>) to tap water. Irrigation volumes were  
181 applied every two days.

182 EMI readings - in vertical magnetic dipoles configurations - were collected by using a Geonics  
183 EM38 device (Geonics Limited, Ontario, Canada). The EM38 operates at a frequency of 14.6 kHz  
184 with a coil spacing of 1 m, and with a nominal measurement depth of ~1.5 m (McNeill, 1980).  
185 The lateral footprint of the EM38 measurement can be considered approximately equal to the  
186 vertical one. Thus, the  $\sigma_b$  seen by the EMI, in a given depth-layer, necessarily differs from that  
187 seen by a TDR probe at the same depth-layer, due to the very different spatial resolutions.

188 At the beginning of the measurement campaign, the EMI sensor was “nulled” according to the  
189 manufacturer’s manual. Readings were taken just after each irrigation application at 1 m step,  
190 along the central line of each transect, for an overall total of 26 soundings per transect. Multi-  
191 height EM38 readings were acquired at heights of 0.0, 0.2, 0.4 and 0.6 m from the ground.



192 Taking measurements just after irrigation allowed relatively time-stable water contents to be  
193 assumed at each site throughout the monitoring phases.

194 Just after the EM38 measurements, a TDR probe was inserted vertically at the soil surface in 26  
195 locations, each corresponding to the central point of an EM38 reading. A Tektronix 1502C cable  
196 tester (Tektronix Inc., Beaverton, OR) was used in this study. It enables simultaneous  
197 measurement of water content  $\theta$  and bulk electrical conductivity  $\sigma_b$  of the soil volume explored  
198 by the probe (Heimovaara et al. 1995; Robinson and Friedman 2003; Coppola et al. 2011;  
199 Coppola et al. 2015). The TDR transmission line consisted of an antenna cable (RG58, 50  $\Omega$   
200 characteristic impedance, 2 m long and with 0.2  $\Omega$  connector impedance) and three-wire  
201 probes, 0.25 m long, 0.07 m internal distance, and 0.005 m in diameter. The TDR probe was not  
202 embedded permanently at fixed depths along the soil profile to avoid any potential disturbance  
203 to the EMI acquisitions. The TDR readings were taken at three different depth intervals (0.0-  
204 0.2, 0.2-0.4, 0.4-0.6 m). After the measurements at the surface (0.0-0.2 m), a trench was dug up  
205 to 0.2 m depth. TDR probes were then inserted vertically for the additional collection of the  
206 data in the interval 0.2-0.4 m, after which the trench was deepened up to 0.4 m and readings  
207 were taken at 0.4-0.6 m. The  $\sigma_{b,TDR}$  readings were used for the calibration of the EM38 inversion  
208 results.

209

210 Data Handling

211 *Multi-height EMI readings inversion*

212 Nonlinear 1D forward modeling, which predicts multi-height EMI readings from a loop-loop  
213 device, can be obtained by suitable simplification of Maxwell's equations that takes the  
214 symmetry of the problem into account. This approach is described in detail in (Hendrickx et al.  
215 2002), and is based on a classical approach extensively described in the literature (Wait 1982;

216 Ward and Hohmann 1988). The predicted data are functions of the electrical conductivity and  
 217 the magnetic permeability in a horizontally layered medium.

218 When the coils of the recording device are vertically oriented with respect to the ground  
 219 surface, the reading at height  $h$  can be expressed by using the integral:

$$-\rho^3 \int_0^{\infty} \lambda^2 e^{-2h\lambda} R_0(\lambda) J_0(\rho\lambda) d\lambda, \quad (1)$$

220 where  $\rho$  denotes the distance between the coils,  $J_0(\lambda)$  is the Bessel function of the first kind  
 221 of order 0, and  $R_0(\lambda)$  is a complex valued function which depends upon the electromagnetic  
 222 properties of the ground layers. A similar expression is valid also when the coils are horizontally  
 223 aligned. Hence the dependence of the measured data on the electrical conductivity  $\sigma_k$ , of the  
 224 (homogeneous)  $j$ -th layer is incorporated into the function  $R_0(\lambda)$ . We discretize the problem  
 225 with  $n$  layers whose characteristic parameters  $\sigma_j$  (with  $j = 1, \dots, n$ ) are the unknowns we invert  
 226 for. In the present research, we neglect any dependence of the electromagnetic response on  
 227 magnetic permeability as we assume it is fixed and equal to the permeability of empty space. In  
 228 principle, it is possible to consider two measurements for each location: one for the horizontal  
 229 and one for the vertical configuration of the transmitting and receiving loops. In this case, the  
 230 data used as inputs for the inversion are  $2*m$ , where  $m$  is the number of heights  $h_1, h_2, \dots, h_m$   
 231 where the measurements are performed.

232 A least squares data fitting approach leads to the minimization of the function:

$$f(\sigma) = \frac{1}{2} \sum_{i=1}^{2m} r_i^2(\boldsymbol{\vartheta}), \quad (2)$$

233 where  $\boldsymbol{\sigma} = (\sigma_1, \dots, \sigma_n)^\top$ , and  $r_i^2(\boldsymbol{\vartheta})$  is the misfit between the  $i$ -th measurement and the  
 234 corresponding forward modeling prediction based on Eq. 1.

235 We solve the nonlinear minimization problem by the inversion procedure described in Deidda,  
236 Fenu, and Rodriguez (2014). The algorithm is based on a damped regularized Gauss-Newton  
237 method. The problem is linearized at each iteration by means of a first order Taylor expansion.  
238 The use of the exact Jacobian (whose expression is detailed in Deidda, Fenu, and Rodriguez,  
239 2014) makes the computation faster and more accurate than using a finite difference  
240 approximation. The damping parameter is determined in order to ensure both the convergence  
241 of the method and the positivity of the solution. The regularized solution to each linear  
242 subproblem is computed by the truncated generalized singular value decomposition (TGSVD -  
243 Díaz de Alba and Rodriguez, 2016) employing different regularization operators. Besides the  
244 classical regularization matrices based on the discretization of the first and second derivatives,  
245 to further improve the spatial resolution of EMI inversion results in all the cases characterized  
246 by sharp interfaces, we tested a nonlinear regularization stabilizer promoting the  
247 reconstruction of blocky features (Zhdanov, Vignoli, and Ueda 2006; Ley-Cooper et al. 2015;  
248 Vignoli et al. 2015; Vignoli et al. 2017). The advantage of this relatively new regularization is  
249 that, when appropriate prior knowledge about the medium to reconstruct is available, it can  
250 mitigate the smearing and over-smoothing effects of the more standard inversion strategies.  
251 This, in turn, can make the calibration of the EMI data against the TDR data more effective. For  
252 this reason, in the following, the EMI results used for our assessments are those inferred by  
253 means of this sharp inversion. The differences between the “standard” smooth (based on the  
254 first derivative) reconstruction and the sharp one are clearly shown in Figs 2 and 4. In all cases,  
255 the inversions are performed with a 100-layer homogeneous discretization, down to 8 m, with  
256 fix interfaces. We opted for such a parameterization to be able to: (i) control the inversion  
257 results by acting merely on the regularization parameters, and (ii) remove the regularization  
258 effects possibly originated by the discretization choice (e.g., the number of layers, interfaces

259 locations). In this way, it was possible to use an automatic strategy for the selection of the  
260 regularization parameters. In Fig.s 2 and 4, the sharp results (upper panels) associated with the  
261 cases 100-6dS and 50-6dS are compared against the corresponding smooth inversions (middle  
262 panels). Even if the data misfit levels largely match (lower panels in Fig.s 2 and 4, but also Fig.s  
263 3 and 5), the two inversion strategies produce reconstructions that differ significantly. This is  
264 due to the inherent ill-posedness of the EMI inversion. By considering solely the geophysical  
265 observations, it is impossible to decide which model is the best. In this research, based on the  
266 fact that, just after the irrigation, the effect of the water is supposed to remain localized in the  
267 shallowest portion of the soil section, the sharp inversion was found to provide more reliable  
268 results. Moreover, to some extent, the general better agreement of the data calculated from  
269 the sharp model supports the idea that the electrical properties distributions are better  
270 inferred via the sharp regularization. In any case, since in this research we calibrate the EMI-  
271 derived models (and not the data), the final calibrated result will reflect the assumptions made  
272 in the first place when the EMI data are inverted (specifically, the regularization assumptions).

273 A possible alternative way to still effectively use the TDR data to calibrate the EMI  
274 measurements (and not the associated conductivity model) could consist in performing the  
275 calibration in the data-space (and not in the model-space). In this case, the measured TDR  
276 conductivity could be used as input model to calculate the  $EC_a$  response of the EMI device  
277 actually used. In turn, this calculated  $EC_a$  response can be compared against the measured EMI  
278 data and used for their calibration. However, eventually, also this latter data-space calibration  
279 will have to deal with the inversion issues once the calibrated EMI data need to be converted  
280 into conductivities  $\sigma_b$ . In this paper, we chose the model-space calibration strategy as, in  
281 general, in the available EMI inversion codes, it is not always easy to decouple the forward  
282 modelling routines from the overall inversion algorithm. Hence, the discussed approach could

283 be more directly applicable and beneficial for practitioners. On the other hand, it is true that  
284 the data-space calibration naturally takes into account the scale-mismatch between the TDR  
285 and the EMI measurements with no need for any statistical calculation.

286 It is worth noting that the constant magnetic permeability assumption is not always valid.  
287 Inverting for the magnetic permeability is sometimes not only necessary, but it can also provide  
288 an additional tool for soil characterization (e.g., Beard and Nyquist, 1998; Farquharson,  
289 Oldenburg, and Routh, 2003; Deidda, Diaz De Alba, and Rodriguez 2017).

290 For the sake of clarity, hereafter, the  $\sigma_b$  values generated from the EMI data inversion will be  
291 identified explicitly as  $\sigma_{b,EMI}$ .

292

### 293 *TDR-based water content and bulk electrical conductivity*

294 The Tektronix 1502C can measure the total resistance  $R_t$  of the transmission line by:

$$R_t = Z_c \frac{(1 + \rho_\infty)}{(1 - \rho_\infty)} = R_s + R_c \quad (3)$$

295 where:  $R_s$  is the soil's contribution to total resistance and  $R_c$  accounts for the contribution of  
296 the series resistance from the cable; the connector  $Z_c$  is the characteristic impedance of the  
297 transmission line; and  $\rho$  is a reflection coefficient at a very long time, when the waveform has  
298 stabilized.

299 The  $\sigma_b$  value at 25°C can be calculated as (Rhoades and van Schilfgaarde 1976; Wraith et al.  
300 1993):

$$\sigma_{b,25^\circ\text{C}} = \frac{K_c}{Z_c} f_T \quad (4)$$

301 where  $K_c$  is the geometric constant of the TDR probe and  $f_T$  is a temperature correction factor  
302 to be used for values recorded at temperatures other than 25°C. Both  $Z_c$  and  $K_c$  can be

303 determined by measuring  $R_t$  with the TDR probe immersed in a solution with known  
 304 conductivity  $\sigma_b$ . Hereafter, these  $\sigma_b$  measurements will be identified as  $\sigma_{b,TDR}$ .

305

306 *Evaluation of Concordance between  $\sigma_{b,TDR}$  measurements and  $\sigma_{b,EMI}$  estimates*

307 The agreement between  $\sigma_{b,TDR}$  measurements and  $\sigma_{b,EMI}$  estimations in the 0.0-0.6 m range was  
 308 evaluated by the Concordance Correlation Coefficient,  $\rho_L$  :

$$\rho_L = \frac{2s_{xy}}{z_x^2 + z_y^2 + (m_x - m_y)^2} \quad (5)$$

309 where  $m_x$ ,  $m_y$ ,  $s_x$ ,  $s_y$ ,  $s_{xy}$  are means, standard deviations and covariances of the two data series  
 310 ( $x = \sigma_{b,EMI}$ ;  $y = \sigma_{b,TDR}$ ), respectively.

311 Scatter plots of the  $\sigma_{b,EMI}$  and  $\sigma_{b,TDR}$  data series (both original and filtered) were evaluated by  
 312 the line of perfect concordance (1:1 line) and the reduced major axis of the data (RMA)  
 313 (Freedman et al. 1991). The method combines measurements of both precision and accuracy to  
 314 determine how close the two data series are to the line of perfect concordance  $\sigma_{b,EMI} = \sigma_{b,TDR}$ .  
 315 Compared to the classical Pearson correlation coefficient,  $\rho_P$ :

$$\rho_P = \frac{s_{xy}}{s_x s_y}, \quad (6)$$

316  $\rho_L$  not only measures the strength of linear relationship (how close the data in the scatter plot  
 317 are to a line), but also the level of agreement (how close that line is to the line of perfect  
 318 agreement, the 1:1 line). In this sense,  $\rho_L$  may also be calculated as (Cox 2006):

$$\rho_L = \rho_P C_b,$$

$$C_b = \frac{2}{(v+1/v+u^2)}, \quad (7)$$

$$v = s_x / s_y,$$

319 and

$$u = (m_x - m_y) / \sqrt{s_x s_y},$$

320 where  $C_b$  is the bias correction factor measuring how far the best-fit line deviates from the 1:1  
321 line. The maximum value of  $C_b = 1$  ( $0 < C_b < 1$ ) corresponds to no deviation from the line. The  
322 smaller  $C_b$  is, the greater the deviation from the line. In other words,  $C_b$  is a measure of  
323 accuracy (how much the average estimate differs from the average measurement value,  
324 assumed to be the true value) and refers to the systematic error, whereas  $\rho_p$  is a measure of  
325 precision (measures the variability of measurements around their own average) and refers to  
326 the random error. The RMA line is given by:

$$y = (m_y - \beta m_x) + \beta x = \alpha + \beta x. \quad (8)$$

327 This line passes through the means of the x and y values and has slope given by the sign of  
328 Pearson's correlation coefficient,  $\rho_p$ , and the ratio of the standard deviations,  $s$ , of the two  
329 series (Freedman et al. 1991, Corwin and Lesch 2005):

$$\beta = s_y / s_x. \quad (9)$$

330  $\rho_L$  increases in value as (i) the RMA approaches the line of perfect concordance (a matter of  
331 accuracy) and (ii) the data approach the RMA (a matter of precision). In the ideal case of  
332 perfect concordance, the intercept of the RMA,  $\alpha$ , should be 0 and  $\beta$  should be 1. Therefore,  $\alpha$   
333  $\neq 0$  or  $\beta \neq 1$  indicate additive and/or multiplicative biases (location and/or scale shifts). The  
334 concordance was evaluated for the original TDR data, as well as for the filtered TDR data. For  
335 the analysis described in detail later in the paper, it is worth noting that the coefficients  $\alpha$  and  $\beta$   
336 depend only on the statistical characteristics (mean and standard deviation) of the two series,  
337 as  $\alpha = m_y - \beta m_x$  and  $\beta = s_y / s_x$ .

338

339 *Fourier filtering*

340 Because of their relatively small observation volume ( $\sim 10^{-3} \text{ m}^3$ ), TDR sensors provide quasi-  
341 pointlike measurements and are, thus, more effective in capturing small-scale variability (in  
342 water content, solute concentrations) induced by natural soil heterogeneity. Thus, the  
343 variability within a set of TDR readings is expected to originate from a combination of small and  
344 large-scale heterogeneities (high and low spatial frequency components). By contrast, the EMI  
345 measurements (because of the size and physics of the instrumentation) necessarily integrate  
346 out the small-scale variability at the TDR scale of investigation.

347 Hence, in order to make the two datasets comparable, the original spatial TDR data series need  
348 to be filtered to remove the variation from small-scale heterogeneities (recorded only by the  
349 TDR probe). In this way, only the information at a spatial scale equal to or larger than the  
350 observation volume of both sensors is preserved.

351 Thus, a simple filter based on the Fourier Transform (FT) is applied to the TDR series.  
359 So, a low-pass frequency filtering is performed on the TDR data to remove all components  
360 related to the small scale heterogeneities and make it comparable with the EMI measurements.  
361 More specifically, for each transect, we consider the  $\sigma_{b,EMI}$  reconstruction and, for each of its 1D  
362 models, calculate the average conductivity value within each depth interval for which the TDR  
363 data are available (namely: 0.0-0.2 m, 0.2-0.4 m, 0.4-0.6 m). Hence, for each depth interval,  
364 along the entire transect, we can calculate the mean and standard deviation of the conductivity  
365 values retrieved from the EMI observations. Subsequently, this standard deviation (associated  
366 with the EMI data) is compared with the standard deviation of the iteratively low-pass filtered  
367 TDR data for the same depth interval. In this way, an optimal cut-off frequency can be selected  
368 to make the scales of the two kinds of measurements compatible. Figure 6 shows the  
369 comparison between the standard deviations of the EMI and filtered TDR data, for the 50-6dS



370 transect, at 0.2-0.4 m depth. In this specific case, the selected cut-off frequency to filter the  
371 TDR data is 0.313 cycles/m, corresponding to a 3.2 m range. This is not surprising at this is of  
372 the order of magnitude of the footprint of the EMI measurements.

373

## 374 **Results and Discussion**

375 Hereafter, the original and filtered data will be respectively labeled ORG and FLT. The graphs on  
376 the top panels in Fig. 7 compare  $\sigma_{b,TDR}$  measured by TDR against the corresponding conductivity  
377  $\sigma_{b,EMI}$  retrieved by the EMI (sharp) inversion for the all the transects. From the left, the graphs  
378 refer respectively to the transects identified as 100-6dS, 50-6dS, 100-1dS and 50-1dS. All plots  
379 show the data for the entire investigated profile between 0.0 and 0.6 m, together with the line  
380 of perfect concordance (1:1, black line), and the main regression axis (MRA, red line).

381 The general conclusion is that, in all four transects, and for all three considered depth-layers,  
382 the  $\sigma_{b,EMI}$  values underestimate the  $\sigma_{b,TDR}$  measurements, such that the MRA line generally lies  
383 above the 1:1 line. Not surprisingly, the EMI result seems quite insensitive to TDR variability.  
384 Also, a considerable scatter around the MRA line may be observed for all transects.

385 Table 1 shows the MRA coefficients ( $C_b$ ,  $\alpha$ ,  $\beta$ ), as well as the Pearson,  $\rho_p$ , and the concordance  
386 correlation,  $\rho_L$ , for the three depth-layers and for all four transects investigated. We recall that  
387 the bias correction factor  $C_b$ , the slope  $\beta$ , and the intercept  $\alpha$  should be respectively close to 1,  
388 1 and 0, for the MRA to approximate the line of perfect concordance. For all the transects and  
389 all the depth-layers considered, the parameters confirm the relatively loose relationship  
390 between  $\sigma_{b,EMI}$  and  $\sigma_{b,TDR}$  already observed in the graphs, both in terms of accuracy (the distance  
391 of the MRA line from the 1:1) and precision (the data scatter around the MRA line).

392 Von Hebel et al. (2014) found a similar behavior when comparing their EMI and ERT datasets. In  
393 that case, the  $EC_a$  values measured by EMI systematically underestimated the  $EC_a$  generated by

394 applying EMI forward modeling to the  $\sigma_b$  distribution retrieved by ERT. To remove the bias, the  
395 authors performed a linear regression between measured and predicted  $EC_a$  after applying a  
396 ten-term moving average to the original data. By using the regression coefficients, all the  
397 measured  $EC_a$  values were converted to ERT-calibrated  $EC_a$  values.

398 Here, we follow a different approach to calibrate the  $\sigma_{b,EMI}$  values against the  $\sigma_{b,TDR}$   
399 measurements based on the MRA coefficients and, so, on the statistical parameters (mean and  
400 standard deviation) of the two data series. Specifically, the present approach looks for a  
401 systematic correction of the bias based on well-defined statistical sources of the discrepancies.  
402 In short, the proposed method performs the calibration in the  $\sigma_b$  model-space, instead of the  
403  $EC_a$  data-space. Our model-space approach mostly relies on the statistical parameters of the  
404 two series. Analyzing the role of these statistics in explaining the discrepancies between EMI  
405 and TDR data observed in Fig. 7a may help to understand how they can be effectively used for  
406 making EMI results directly comparable with the TDR values.

407 In nearly all of the graphs in the top panels in Fig. 7, the discrepancies between  $\sigma_{b,EMI}$  and  $\sigma_{b,TDR}$   
408 values can be decomposed in the following components:

- 409 1. The distance along the  $\sigma_{b,EMI}$  axis of the MRA line from the 1:1 line, that is the difference  
410 between the  $\sigma_{b,EMI}$  and the  $\sigma_{b,TDR}$  means.
- 411 2. The difference in the slope of the MRA and of the 1:1 lines, which stems from the different  
412 variability of  $\sigma_{b,EMI}$  (its standard deviation) and that of  $\sigma_{b,TDR}$ . We recall here that the slope of  
413 the MRA is just the ratio of the two standard deviations,  $\hat{\beta} = s_y / s_x$ .
- 414 3. The scatter of the data around the MRA line, which may come from different sensors' noise  
415 and the influence of surrounding conditions (e.g., temperature).

416 Below, we analyze in detail the role of all these three points with the support of the measured  
417 data.

418 1. The distance of the MRA from the 1:1 line is mostly due to the difference in the observed  
419 means. The plot in Figure 8a compares the means for the two original series (squares-solid line  
420 for TDR, circles-dashed line for EMI). Figure 8b reports the same comparison on a 1:1 plot  
421 (triangles-solid regression line). The mean values confirm the general underestimation of TDR  
422 by the EMI data. However, the trends are evidently similar, which is reflected in the high  
423 correlation between the means of the two series, with a significantly high  $R^2=0.81$ . This high  
424 correlation has very positive implications from an applicative point of view, since, after the  
425 calibration in a specific site, it allows the EMI mean to be inferred given the mean of TDR  
426 readings taken in that soil, and thus provides the possibility to migrate the more reliable TDR  
427 information across the larger area that can be practically investigated during an EMI survey.

428 2. The different slope of the two lines has to be ascribed to the different variability of the two  
429 series. Figure 9a compares the standard deviations for the two original series (squares-solid line  
430 for TDR, circles-dashed line for EMI). Figure 9b reports the same comparison on a 1:1 plot  
431 (triangles-solid regression line). Conceptually, the different variability of the two series can be  
432 related to the different sensor observation volumes (originated from the different spatial  
433 sensitivity of the sensors - Coppola et al. 2016). For TDR probes, most of the measurement  
434 sensitivity is close to the rods (Ferré et al. 1998b). Conversely, the spatial resolution of inverted  
435 EMI  $EC_a$  values may be much lower as the resolution of the EMI result depends on the physics  
436 of the method, the specifications (and configuration) of the recording device, and the  
437 regularization strategy applied during the inversion. Thus, the EMI is generally unable to  
438 capture the small-scale variability seen by the TDR. For our calibration purposes, it is important  
439 to make the variability of EMI and TDR conductivities actually comparable. As discussed by

440 Coppola et al., 2016, a possible method can consist in filtering out the high frequency  
441 components (at small spatial scale) of the original TDR data, while retaining the lower  
442 frequency information. This corresponds to keep the information at a spatial scale larger than  
443 the observation volume of the TDR sensor and attuned with the resolution of the  $\sigma_{b,EMI}$   
444 distribution. From a practical point of view, this makes sense, as TDR readings are often “too  
445 local” to actually represent the macroscopic physical characteristics of interest for applications  
446 (water content, solute concentrations). The volume explored by a TDR probe may, or may not,  
447 include preferential channels (Mallants et al. 1994; Oberdörster et al. 2010), stones (Coppola et  
448 al. 2011; Coppola et al. 2013), small-scale changes in the texture and structure (Coppola et al.  
449 2011), which can make the interpretation of local measurements difficult for practical  
450 applications. In this sense, EMI’s removal of these small-scale effects may be desirable from a  
451 management perspective. Consistently, the original TDR data are conditioned via a low-pass  
452 filtering, as described in the Data Handling section. The filtering results, in terms of standard  
453 deviations, are reported in Fig. 9a (crosses-dashed line) and Fig. 9b (squares-dashed regression  
454 line). As expected, the low-pass filter makes the standard deviations much closer (almost  
455 overlapping) in all transects and all considered depth-layers. The regression improved  
456 significantly from 0.25 for the original data to 0.78 after the TDR data filtering.

457 3. The scatter is consistently reduced by the spatial filtering (as similarly discussed in Von Hebel  
458 et al., 2014).

459

460 Eventually, the calibrated  $\sigma_{b,EMI}^{rg}$  distribution (superscript *rg* means: EMI data after regression)

461 can then be obtained from the original  $\sigma_{b,EMI}$  via the linear mapping:

$$462 \quad \sigma_{b,EMI}^{rg} = \alpha + \beta \sigma_{b,EMI}, \quad (10)$$

463 where the coefficients  $\alpha$  and  $\beta$  can be easily calculated from the means and standard  
 464 deviations of the EMI results and the filtered TDR data. Thus, if  $m_{EMI}$  and  $m_{TDR(FLT)}$ , and  $s_{EMI}$  and  
 465  $s_{TDR(FLT)}$  are, respectively, the means and the standard deviations of the original  $\sigma_{b,EMI}$  EMI data  
 466 and of the filtered  $\sigma_{b,TDR(FLT)}$  TDR data, the MRA line coefficients can be expressed as  
 467  $\alpha = m_{TDR(FLT)} - \beta m_{EMI}$  and  $\beta = s_{TDR(FLT)} / s_{EMI}$ .

469 The bottom panels in Fig. 7 show the results of the application of the linear mapping. In  
 470 particular, they compare the calibrated EMI data (EMI rg) with the filtered TDR (TDR FLT)  
 471 measurements. The MRA parameters and the concordance coefficients in the case of filtered  
 472 TDR data are reported in Table 2. Clearly, considering the (calibrated) EMI and (filtered) TDR  
 473 standard deviations turns the MRA line to be practically matching the 1:1 line, with the  
 474 coefficient  $\beta$  approaching to 1. Moreover, from Table 2, the improvement of the bias  $C_b$  and the  
 475 concordance  $\rho_L$  is generally significant. On the other hand, the Pearson's correlation  $\rho_p$  is not  
 476 influenced by the recalibration as the proposed approach deals with the statistics of the data  
 477 series rather than the single data. Thus, after the application of the low-pass filter to the TDR  
 478 data, the coefficient  $\beta$  is close to 1, and the calibration turns out to be (almost) a simple shift of  
 479 the inverted  $\sigma_{b,EMI}$ . The amount of this shift is equal to the difference between the mean values  
 480  $m_{TDR(FLT)}$  and  $m_{EMI}$ . To summarize, the TDR filtering allows removing the outlier values generated  
 481 by the small scale variability and preserving the information content necessary to properly  
 482 calculate the shift required for the absolute calibration of the EMI inversion results.

483 Figure 10 shows, on the left, the original  $\sigma_{b,EMI}$  distribution to be compared against the  $\sigma_{b,EMI}^{rg}$   
 484 results (on the right) obtained through the application of the linear transformation in Eq. 10.  
 485 The calibrated transects preserves the spatial variability of the original EMI inversions, but are

486 now characterized by value ranges that are more realistic (as they are obviously closer to the  
487 TDR measurements assumed to be more representative of the real soil conditions).

488 As already discussed, the high correlation of the means and the standard deviations of the two  
489 series are central for this procedure to be of practical interest. In short, the procedure can be  
490 summarized as follows: (i) An area is monitored via EMI survey and a few TDR calibration  
491 measurements are collected concurrently. (ii) The availability of the two different datasets  
492 allows performing the regression for the mean and the standard deviation of the original EMI  
493 inversion results and the filtered TDR data, like those shown in Fig.s 8b and 9b. (iv) These  
494 statistical parameters can be promptly used for the calculation of the coefficients  $\alpha$  and  $\beta$  to be  
495 inserted into Eq. 10. (v) The original EMI inversion results are not always reliable when  
496 compared with the direct measurements obtained by using a TDR probe. Rather, they only  
497 contain the low-frequency information supplied by TDR (most likely, together with some shifts  
498 connected with the poor absolute calibration of the EMI system and/or the working conditions,  
499 e.g., the temperature). Thus, for quantitative analyses, it may be crucial to transform the  
500 original EMI result  $\sigma_{b,EMI}$  into a new, calibrated section  $\sigma_{b,EMI}^{rg}$  by means of the linear mapping  
501 in Eq. 10.

502 The proposed workflow enables us to translate the original non-calibrated  $\sigma_{b,EMI}$  data into the  
503 actual  $\sigma_b$  we would collect in ideal conditions, and which would perfectly match “low-  
504 resolution” TRD measurements.  $\sigma_{b,EMI}^{rg}$  is our best possible estimation of the true electrical  
505 conductivity at the scale of investigation of the EMI survey: it is the original  $\sigma_{b,EMI}$  after the  
506 application of the appropriate rescaling and shifts deduced by the more reliable and absolutely  
507 calibrated TDR measurements.

508

509 **Conclusions**

510 The objective of the paper is to infer the bulk electrical conductivity distribution in the root  
511 zone from multi-height (potentially non-calibrated) EMI readings. TDR direct measurements are  
512 used as ground-truth  $\sigma_b$  data to evaluate the correctness of the  $\sigma_b$  estimations generated by  
513 EMI inversion. For all four transects and for all three depth-layers considered in this study, the  
514  $\sigma_{b,EMI}$  values underestimate the  $\sigma_{b,TDR}$  measurements, such that the MRA line generally lies  
515 above the 1:1 line. Also, a considerable scatter around the MRA line was observed for all  
516 transects.

517 The proposed analysis allows discussing the physical reasons for the differences between EMI-  
518 and TDR-based electrical conductivity and developing an approach to calibrate the original  
519  $\sigma_{b,EMI}$  by using the  $\sigma_{b,TDR}$  measurements. Our approach is based on the MRA coefficients and,  
520 hence, on the statistical parameters (mean and standard deviation) of the two series.  
521 Specifically, the approach looks for a systematic correction of the bias based on well-defined  
522 statistical sources of the discrepancies. A low-pass filtering has been carried out on the TDR  
523 data to obtain a significantly high correlation between the standard deviations of the two data  
524 series. After that, a simple linear transformation can be applied to the originally inverted EMI  
525 section  $\sigma_{b,EMI}$  to get a calibrated  $\sigma_b$  result.

526 The proposed strategy lies on the assumption that TDR direct measurements supply absolutely  
527 calibrated observations of the electrical conductivity of the soil and can be effectively used to  
528 calibrate the conductivity distributions inferred from EMI data. The availability of EMI  
529 calibrated data paves the way to reliable reconstructions of the electrical conductivity  
530 distribution over large areas (typical for EMI surveys, but not for TDR campaigns) unaffected by  
531 the usual EMI miscalibrations. This, in turn, can result in the possibility of effective time-lapse  
532 surveys and/or in consistent merging of subsequent surveys.

533 On the other hand, the proposed statistical workflow for making the TDR measurement  
534 comparable with the associated EMI results provides a more sophisticated approach than  
535 simple smoothing to upscale the TDR data. Thus, from the opposite perspective, the approach  
536 in question can be used to tackle the problems connected with handling the TDR data  
537 characterized by excessively high spatial resolution.

538

### 539 **References**

540 Abdu, H., D.A. Robinson, and S.B. Jones. 2007. Comparing bulk soil electrical conductivity  
541 determination using the DUALEM-1S and EM38-DD electromagnetic induction instruments. *Soil*  
542 *Sci. Soc. Am. J.* 71 (1):189-196. doi: 10.2136/sssaj2005.0394.

543

544 Amezketa, E. 2006. An integrated methodology for assessing soil salinization, a pre-condition  
545 for land desertification. *J. Arid Environ.* 67 (4):594-606. doi: 10.1016/j.jaridenv.2006.03.010.

546

547 Beard, L. P., and J. E. Nyquist. 1998. Simultaneous inversion of airborne electromagnetic data  
548 for resistivity and magnetic permeability. *Geophysics* 63 (5): P1556-1564.

549

550 Bechtold, M., J.A. Huisman, L. Weihermüller, and H. Vereecken. 2010. Accurate  
551 determination of the bulk electrical conductivity with the TDR100 cable tester. *Soil Sci. Soc.*  
552 *Am. J.* 74, 495–501

553

554 Borchers, B., T. Uram, and J.M.H. Hendrickx. 1997. Tikhonov regularization of electrical  
555 conductivity depth profiles in field soils. *Soil Sci. Soc. Am. J.* 61 (4):1004-1009. doi:

556 10.2136/sssaj1997.03615995006100040002x.



557

558 Cassiani, G., N. Ursino, R. Deiana, G. Vignoli, J. Boaga, M. Rossi, M. T. Perri, M. Blaschek, R.

559 Duttmann, S. Meyer, R. Ludwig, A. Saddu, P. Dietrich, and U. Werban. *Vadose Zone J.*

560 doi:10.2136/vzj2011.0195

561

562 Coppola, A., G. Dragonetti, A. Comegna, N. Lamaddalena, B. Caushi, M.A. Haikal, and A. Basile.

563 2013. Measuring and modeling water content in stony soils. *Soil Till. Res.* 128:9-22.

564

565 Coppola, A., K. Smettem, A. Ajeel, A. Saeed, G. Dragonetti, A. Comegna, N. Lamaddalena, and A.

566 Vacca. 2016. Calibration of an electromagnetic induction sensor with time-domain

567 reflectometry data to monitor rootzone electrical conductivity under saline water irrigation.

568 *Eur. J. of Soil Sci.* 67 (6):737-748. doi: 10.1111/ejss.12390.

569

570 Coppola, A., N. Chaali, G. Dragonetti, N. Lamaddalena, and A. Comegna. 2015. Root uptake

571 under non-uniform root-zone salinity. *Ecohydrology.* 8 (7):1363-1379. doi: 10.1002/eco.1594.

572

573 Coppola, A., A. Comegna, G. Dragonetti, M. Dyck, A. Basile, N. Lamaddalena, M. Kassab, and V.

574 Comegna. 2011. Solute transport scales in an unsaturated stony soil. *Adv. Water Resour.* 34

575 (6):747-759. doi: <http://dx.doi.org/10.1016/j.advwatres.2011.03.006>.

576

577 Corwin, D.L., and S.M. Lesch. 2005. Apparent soil electrical conductivity measurements in

578 agriculture. *Comput. Electron. Agr.* 46 (1):11-43.

579

580 Cox, N.J. 2006. Assessing agreement of measurements and predictions in geomorphology.  
581 *Geomorphology*. 76 (3):332-346.  
582

583 Dalton, F. N., W. N. Herkelrath, D. S. Rawlins, and J. D. Rhoades. 1984. Time domain  
584 reflectometry: Simultaneous measurement of soil water content and electrical conductivity  
585 with a single probe. *Science* 224, 989–990.  
586

587 Deidda, G.P., E. Bonomi, and C. Manzi. 2003. Inversion of electrical conductivity data with  
588 Tikhonov regularization approach: some considerations. *Ann. Geophys.*  
589

590 Deidda, G.P., C. Fenu, and G. Rodriguez. 2014. Regularized solution of a nonlinear problem in  
591 electromagnetic sounding *Inverse Probl.* 30 (12):125014.  
592

593 Deidda, G.P., P. Diaz De Alba, and G. Rodriguez. 2017. Identifying the magnetic permeability in  
594 multi-frequency EM data inversion. *Submitted*.  
595

596 Díaz de Alba, P., and G. Rodriguez. 2016. Regularized Inversion of Multi-Frequency EM Data in  
597 Geophysical Applications. In *Trends in Differential Equations and Applications*, 357-369.  
598 Springer.  
599

600 Doolittle, J.A., and E.C. Brevik. 2014. The use of electromagnetic induction techniques in soils  
601 studies. *Geoderma* . 223:33-45.  
602

603 Farquharson, C. G., Oldenburg, D. W., and Routh, P. S. 2003. Simultaneous 1D inversion of loop-  
604 loop electromagnetic data for both magnetic susceptibility and electrical conductivity.  
605 *Geophysics*. 68, 1857–1869.  
606

607 Ferré, P.A., J. D. Redman, D.L. Rudolph, and R.G. Kachanoski. 1998a. The dependence of the  
608 electrical conductivity measured by time domain reflectometry on the water content of a sand.  
609 *Water Resour. Res.* 34 (5):1207-1213  
610

611 Ferré, P.A., J.H. Knight, D.L. Rudolph, and R.G. Kachanoski. 1998b. The sample areas of  
612 conventional and alternative time domain reflectometry probes. *Water Resour. Res.* 34  
613 (11):2971-2979.  
614

615 Fiandaca, G., J. Doetsch, G. Vignoli, and E. Auken. 2015. Generalized focusing of time-lapse  
616 changes with applications to direct current and time-domain induced polarization inversions.  
617 *Geophys. J. Int.* 203 (2):1101-1112. doi: 10.1093/gji/ggv350.  
618

619 Freedman, D., R. Pisani, R. Purves, and A. Adhikari. 1991. *Statistics* (2nd ed.). New York: W. W.  
620 Norton.  
621

622 Gebbers, R., E. Lück, M. Dabas, and H. Domsch. 2009. Comparison of instruments for  
623 geoelectrical soil mapping at the field scale. *Near Surf. Geophys.* 7 (3):179-190. doi:  
624 10.3997/1873-0604.2009011  
625

626 Günther, T. 2011. Timelapse ERT inversion approaches and their applications. *Geoelectric*  
627 *Monitoring*:91.  
628  
629 Heimovaara, T.J., A.G. Focke, W. Bouten, and J.M. Verstraten. 1995. Assessing temporal  
630 variations in soil water composition with time domain reflectometry. *Soil Sci. Soc. Am. J.* 59  
631 (3):689-698. doi: 10.2136/sssaj1995.03615995005900030009x.  
632  
633 Hendrickx, J.M.H., B. Borchers, D.L. Corwin, S.M. Lesch, A.C. Hilgendorf, and J. Schlue. 2002.  
634 Inversion of soil conductivity profiles from electromagnetic induction measurements. *Soil Sci.*  
635 *Soc. Am. J.* 66 (3):673-685. doi: 10.2136/sssaj2002.6730.  
636  
637 Huisman, J.A., C. P. Lin, L. Weihermüller, H. Vereecken. 2008. Accuracy of Bulk Electrical  
638 Conductivity Measurements with Time Domain Reflectometry. *Vadose Zone J.* 7, 426–433  
639  
640 Koestel, J., A. Kemna, M. Javaux, A. Binley, H. Vereecken. 2008. Quantitative imaging of solute  
641 transport in an unsaturated and undisturbed soil monolith with 3-D ERT and TDR. *Water*  
642 *Resour. Res.* 44, W12411, doi:10.1029/2007WR006755.  
643  
644 Lavoué, F., J. van der Kruk, J. Rings, F. André, D. Moghadas, J.A. Huisman, S. Lambot, L.  
645 Weihermüller, J. Vanderborght, and H. Vereecken. 2010. Electromagnetic induction calibration  
646 using apparent electrical conductivity modelling based on electrical resistivity tomography.  
647 *Near Surf. Geophys.* 8 (6):553-561.  
648

649 Lesch, S.M., J.D. Rhoades, L.J. Lund, and D.L. Corwin. 1992. Mapping soil salinity using  
650 calibrated electromagnetic measurements. *Soil Sci. Soc. Am. J.* 56 (2):540-548. doi:  
651 10.2136/sssaj1992.03615995005600020031x.  
652  
653 Ley-Cooper, A.Y., A. Viezzoli, J. Guillemoteau, G. Vignoli, J. Macnae, L. Cox, and T. Munday.  
654 2015. Airborne electromagnetic modelling options and their consequences in target definition.  
655 *Explor. Geophys.* 46 (1):74-84. doi: 10.1071/eg14045.  
656  
657 Lin, K. 1989. A concordance correlation coefficient to evaluate reproducibility. *Biometrics*:255-  
658 268.  
659  
660 Lin, C.P., C. C. Chung, J. A. Huisman, and S. H. Tang. 2008. Clarification and calibration of  
661 reflection coefficient for time domain reflectometry electrical conductivity measurement. *Soil*  
662 *Sci. Soc. Am. J.* 72, 1033-104072.  
663  
664 Lin, C.P., C. C. Chung, and S. H. Tang. 2007. Accurate time domain reflectometry measurement  
665 of electrical conductivity accounting for cable resistance and recording time. *Soil Sci. Soc. Am. J.*  
666 71,1278–1287.  
667  
668 Mallants, D., M. Vanclooster, M. Meddahi, and J. Feyen. 1994. Estimating solute transport in  
669 undisturbed soil columns using time-domain reflectometry. *Journal Contam. Hydrol.* 17 (2):91-  
670 109. doi: 10.1016/0169-7722(94)90016-7.  
671

672 McNeill, J.D. 1980. Electromagnetic terrain conductivity measurement at low induction  
673 numbers. Geonics Limited Ontario, Canada.  
674

675 Mester, A., J. Van Der Kruk, E. Zimmermann, and H. Vereecken. 2011. Quantitative Two-Layer  
676 Conductivity Inversion of Multi-Configuration Electromagnetic Induction Measurements.  
677 *Vadose Zone J.* 10:1319-1330. doi: 10.2136/vzj2011.0035.  
678

679 Minsley, B.J., B.D. Smith, R. Hammack, J.I. Sams, and G. Veloski. 2012. Calibration and filtering  
680 strategies for frequency domain electromagnetic data. *J. Appl. Geophys.* 80:56-66. doi:  
681 10.1016/j.jappgeo.2012.01.008.  
682

683 Moghadas, D., F. André, J.H. Bradford, J. van der Kruk, H. Vereecken, and S. Lambot. 2012.  
684 Electromagnetic induction antenna modelling using a linear system of complex antenna  
685 transfer functions. *Near Surf. Geophys.* 10 (3):237-247. doi: 10.3997/1873-0604.2012002  
686

687 Noborio, K. 2001. Measurement of soil water content and electrical conductivity by time  
688 domain reflectometry: A review. *Comput. Electron. Agric.* 31:213–237.  
689

690 Nüsch, A.K., P. Dietrich, U. Werban, T. Behrens, and N. Prakongkep. 2010. Acquisition and  
691 reliability of geophysical data in soil science. Paper read at 19th world congress of soil science,  
692 soil solutions for a changing world, Brisbane, Australia.  
693

694 Oberdörster, C., J. Vanderborght, A. Kemna, and H. Vereecken. 2010. Investigating preferential  
695 flow processes in a forest soil using time domain reflectometry and electrical resistivity  
696 tomography. *Vadose Zone J.* 9 (2):350-361.  
697  
698 Pagliara, G., and G. Vignoli. 2006. Focusing inversion techniques applied to electrical resistance  
699 tomography in an experimental tank. In *XI International Congress of the International*  
700 *Association for Mathematical Geology*.  
701  
702 Rhoades, J.D., and D.L. Corwin. 1981. Determining soil electrical conductivity-depth relations  
703 using an inductive electromagnetic soil conductivity meter. *Soil Sci. Soc. Am. J.* 45 (2):255-260.  
704  
705 Rhoades, J.D., and J. van Schilfgaarde. 1976. An electrical conductivity probe for determining  
706 soil salinity. *Soil Sci. Soc. Am. J.* 40 (5):647-651. doi:  
707 10.2136/sssaj1976.03615995004000050016x.  
708  
709 Robinson, D.A., and S.P. Friedman. 2003. A method for measuring the solid particle permittivity  
710 or electrical conductivity of rocks, sediments, and granular materials. *J. Geophys. Res-Sol Ea.*  
711 108 (B2):2076. doi: 10.1029/2001JB000691.  
712  
713 Robinson, D. A., S. B. Jones, J. M. Wraith, D. Or, and S. P., Friedman. 2003. A review of  
714 advances in dielectric and electrical conductivity measurement using time domain  
715 reflectometry. *Vadose Zone J.* 2, 444–475.  
716

717 Robinson, D.A., I. Lebron, S.M. Lesch, and P. Shouse. 2004. Minimizing Drift in Electrical  
718 Conductivity Measurements in High Temperature Environments using the EM-38. *Soil Sci. Soc.  
719 Am. J.*. 68 (2):339-345. doi: 10.2136/sssaj2004.3390.  
720

721 Robinson, D.A., H. Abdu, I. Lebron, and S.B. Jones. 2012. Imaging of hill-slope soil moisture  
722 wetting patterns in a semi-arid oak savanna catchment using time-lapse electromagnetic  
723 induction. *J. Hydrol.* 416–417:39-49. doi:https://doi.org/10.1016/j.jhydrol.2011.11.034.  
724

725 Santos, F.A. Monteiro, J. Triantafilis, K.E. Bruzgulis, and J.A.E. Roe. 2010. Inversion of  
726 Multiconfiguration Electromagnetic (DUALEM-421) Profiling Data Using a One-Dimensional  
727 Laterally Constrained Algorithm. *Vadose Zone J.* 9:117-125. doi: 10.2136/vzj2009.0088.  
728

729 Sheets, K.R., and J.M.H. Hendrickx. 1995. Noninvasive soil water content measurement using  
730 electromagnetic induction. *Water Resour. Res.* 31 (10):2401-2409.  
731

732 Shumway, R.H. 1988. *Applied Time Series Analysis*: Prentice-Hall, Englewood Cliffs, NJ.  
733

734 Sudduth, K.A., S.T. Drummond, and N.R. Kitchen. 2001. Accuracy issues in electromagnetic  
735 induction sensing of soil electrical conductivity for precision agriculture. *Comput. Electron. Agr.*  
736 31 (3):239-264. doi: 10.1016/S0168-1699(00)00185-X.  
737

738 Thomsen, A., K. Schelde, P. Drøschler, F. Steffensen. 2007. Mobile TDR for geo-referenced  
739 measurement of soil water content and electrical conductivity. *Precision Agriculture* 8, 213–223  
740



741 Topp, G. C., M. Yanuka, W. D. Zebchuk, and S. Zegelin. 1988. Determination of electrical  
742 conductivity using time domain Reflectometry: Soil and water experiments in coaxial lines.  
743 *Water Resour. Res.* 24, 945–952.  
744

745 Triantafilis, J., G.M. Laslett, and A.B. McBratney. 2000. Calibrating an electromagnetic induction  
746 instrument to measure salinity in soil under irrigated cotton. *Soil Sci. Soc. Am. J.* 64 (3):1009-  
747 1017. doi: 10.2136/sssaj2000.6431009x.  
748

749 Ursino, N., G. Cassiani, R. Deiana, G. Vignoli and J. Boaga. 2014. Measuring and modeling water-  
750 related soil–vegetation feedbacks in a fallow plot. *Hydrol. Earth Syst. Sci.* 18, 1105–1118.  
751

752 Vignoli, G., G. Fiandaca, A.V. Christiansen, C. Kirkegaard, and E. Auken. 2015. Sharp spatially  
753 constrained inversion with applications to transient electromagnetic data. *Geophys. Prospect.*  
754 63 (1):243-255.  
755

756 Vignoli, G., V. Sapia, A. Menghini, and A. Viezzoli. 2017. Examples of Improved Inversion of  
757 Different Airborne Electromagnetic Datasets Via Sharp Regularization. *J. Environ. Eng. Geophys.*  
758 22 (1):51-61. doi: 10.2113/jeeg22.1.51.  
759

760 Vignoli, G., R. Deiana, and G. Cassiani. 2012. Focused inversion of vertical radar profile (VRP)  
761 travelttime data. *Geophysics.* 77 (1):H9-H18. doi: 10.1190/geo2011-0147.1.  
762

763 Von Hebel, C., S. Rudolph, A.Mester, J.A. Huisman, P. Kumbhar, H. Vereecken, and J. van der  
764 Kruk. 2014. Three-dimensional imaging of subsurface structural patterns using quantitative

765 large-scale multiconfiguration electromagnetic induction data. *Water Resour. Res.* 50 (3):2732-  
766 2748.

767

768 Wait, J.R. 1982. Geo-Electromagnetism. In *Geo-Electromagnetism*, 1-67. Academic Press.

769

770 Ward, S.H., and G.W. Hohmann. 1988. Electromagnetic theory for geophysical applications.  
771 *Electromagnetic methods in applied geophysics*.

772

773 Weerts A. H., J. A. Huisman, and W. Bouten, .2001. Information content of time domain  
774 reflectometry waveforms. *Water Resources Research.* 37 (5), 1291–1299

775

776 Wraith, J.M., B.L. Woodbury, W.P. Inskeep, and S.D. Comfort. 1993. A simplified waveform  
777 analysis approach for monitoring solute transport using time-domain reflectometry. *Soil Sci.*  
778 *Soc. Am. J.* 57 (3):637-642.

779

780 Yao, R., and Jingsong Y. 2010. Quantitative evaluation of soil salinity and its spatial distribution  
781 using electromagnetic induction method. *Agr. Water Manage.* 97 (12):1961-1970. doi:  
782 10.1016/j.agwat.2010.02.001.

783

784 Yu, M., and D.E. Dougherty. 2000. Modified total variation methods for three-dimensional  
785 electrical resistance tomography inverse problems. *Water Resour. Res.* 36 (7):1653-1664.

786

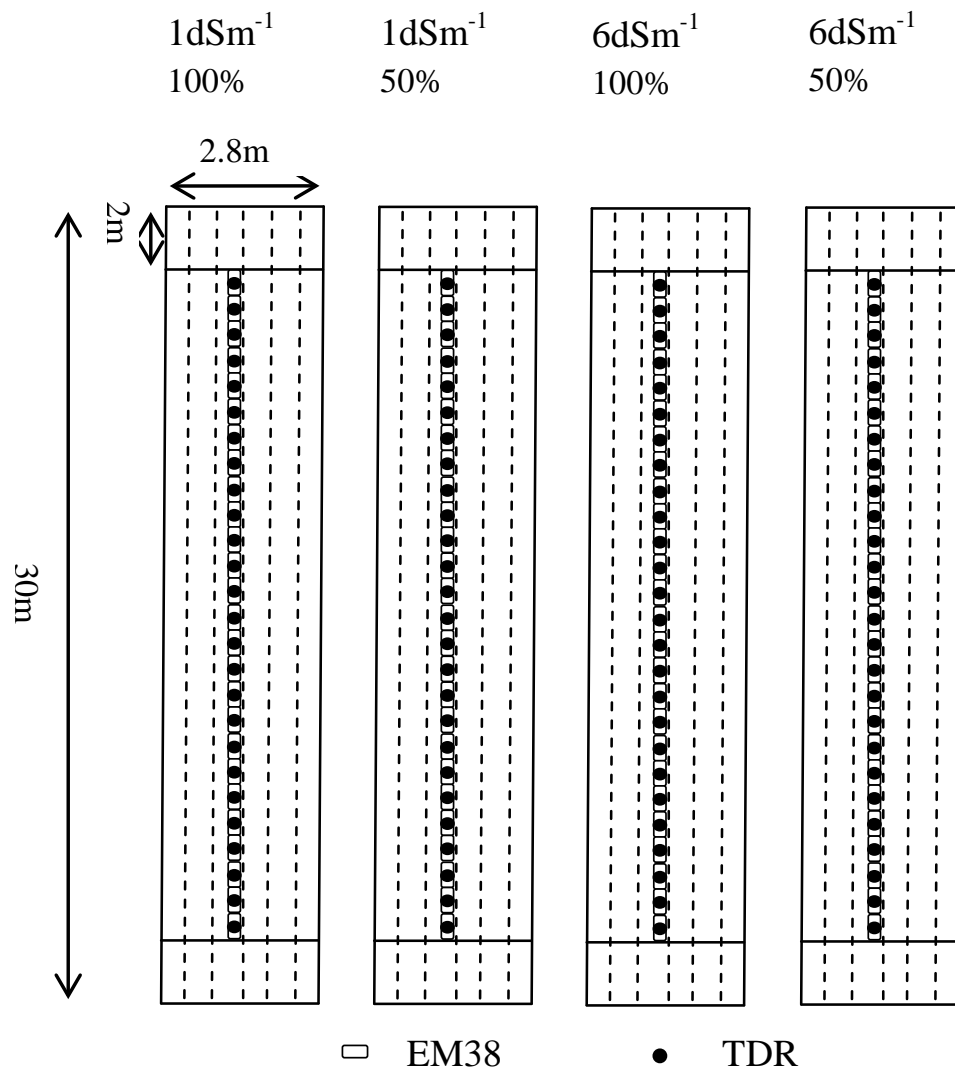
787 Zhdanov, M.S., G. Vignoli, and T. Ueda. 2006. Sharp boundary inversion in crosswell travel-time  
788 tomography. *J. Geophys. Eng.* 3 (2):122.

789

790 Zhdanov, M.S. 2002. Geophysical Inverse Theory and Regularization Problems Methods.

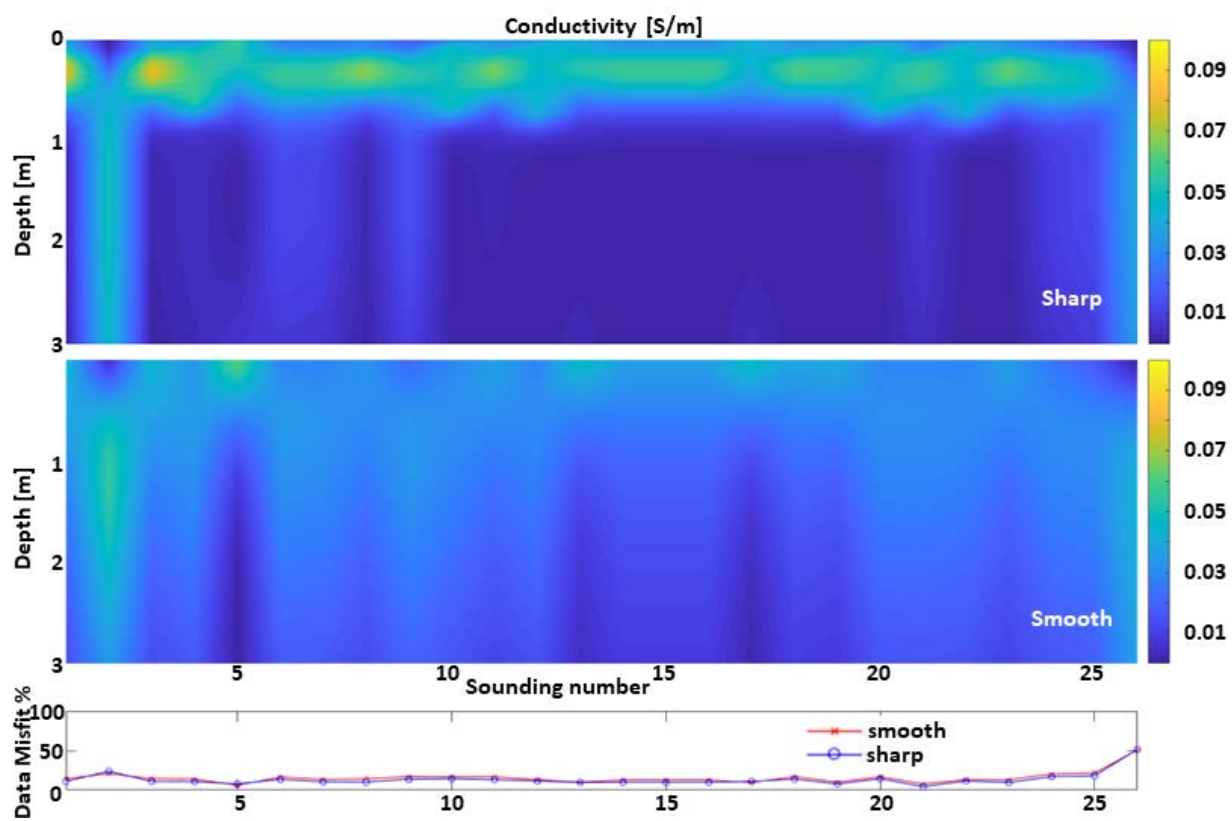
791 Elsevier.

792



793

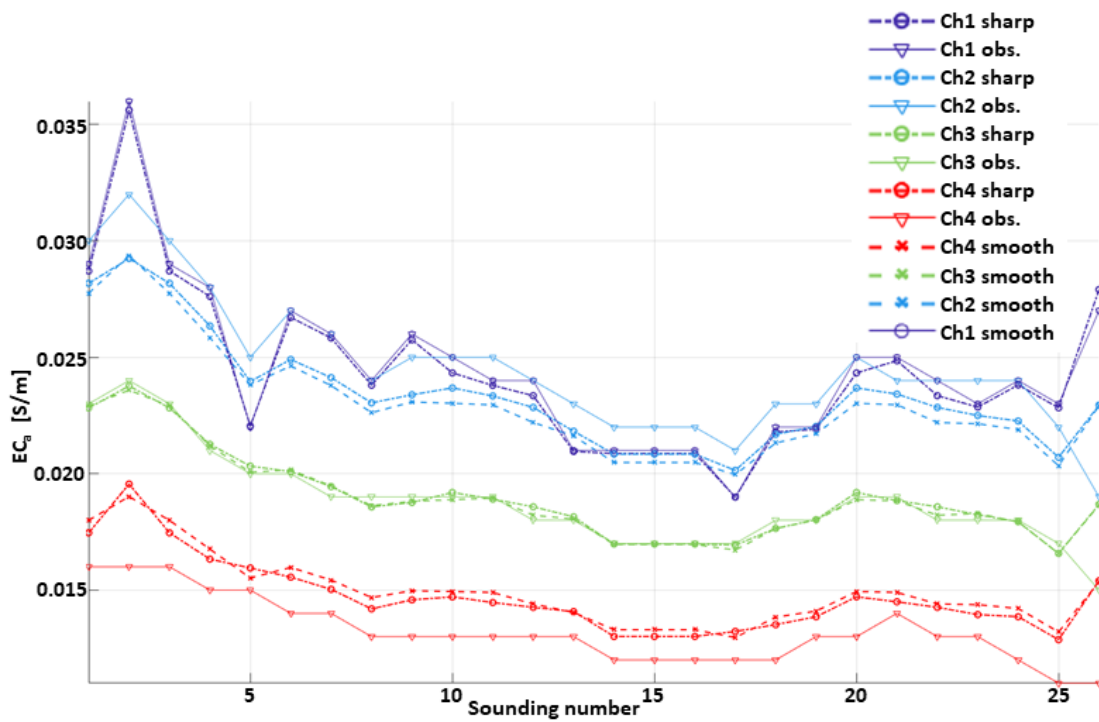
794 Figure 1. Schematic view of the experimental field



795

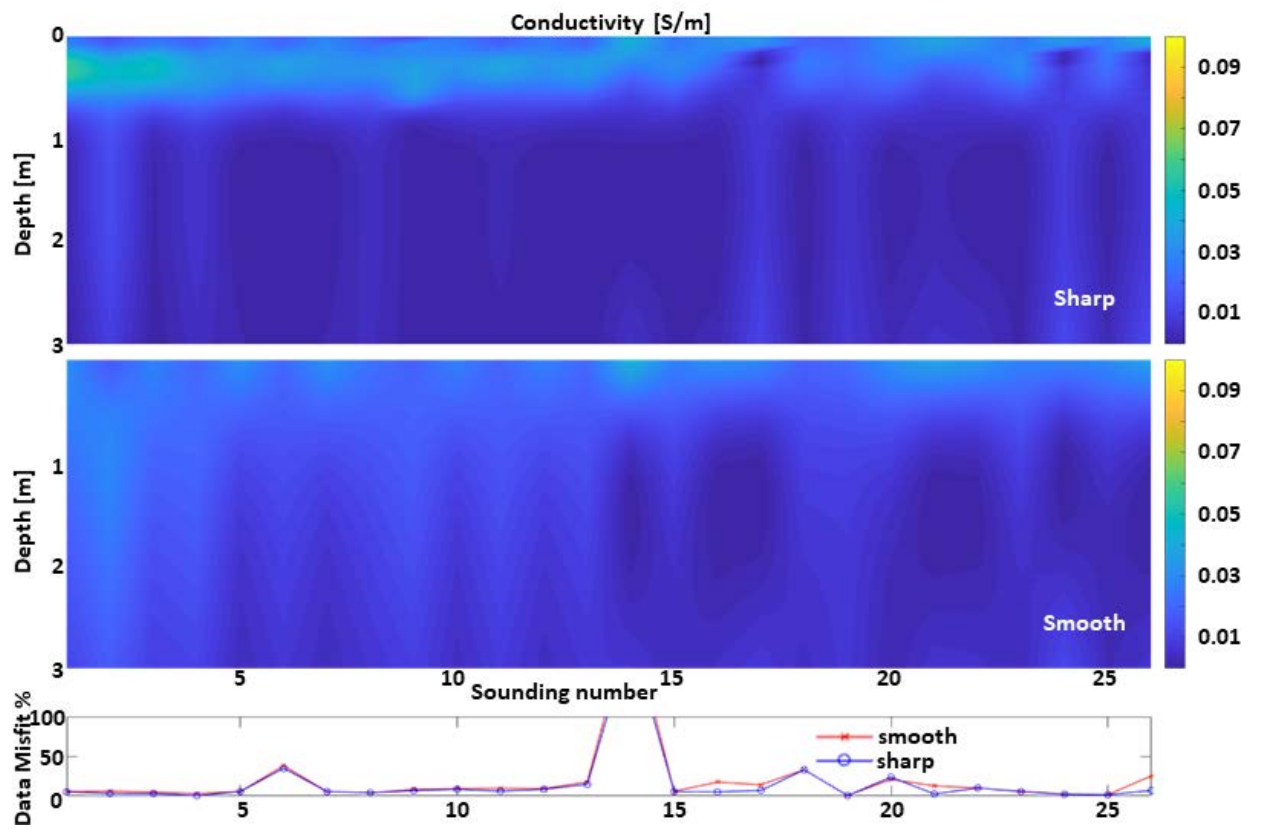
796 Figure 2. Examples of sharp and smooth inversions applied to the dataset 100-6dS. The results

797 are shown together with their corresponding data misfit.



798

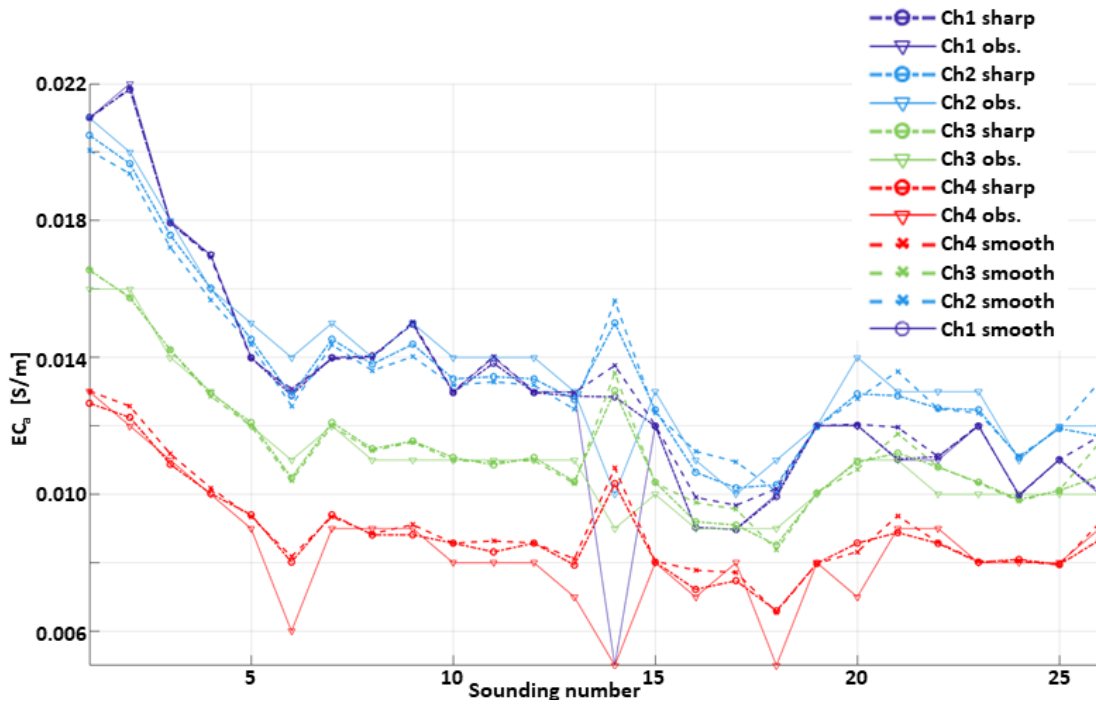
799 Figure 3. Comparison of the data fitting associated with the sharp and smooth inversions  
 800 applied to the dataset 100-6dS (Fig. 2). The calculated data corresponding to the sharp and  
 801 smooth results are shown together with the observations for each of the four measured  
 802 channels (heights).



803

804 Figure 4. Examples of sharp and smooth inversions applied to the dataset 50-6dS. The results

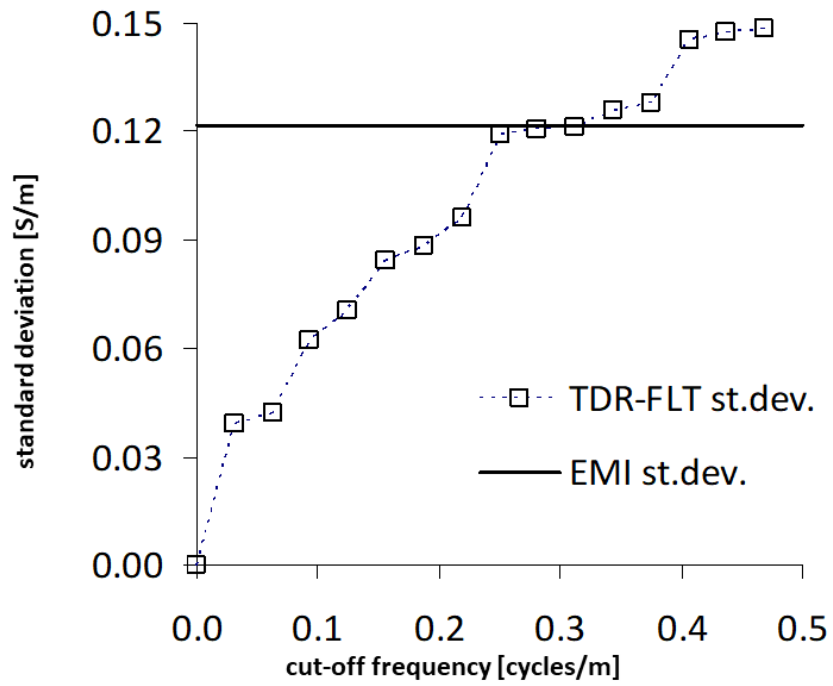
805 are shown together with their corresponding data misfit.



806

807 Figure 5. Comparison of the data fitting associated with the sharp and smooth inversions  
 808 applied to the dataset 50-6dS (Fig. 4). The calculated data corresponding to the sharp and  
 809 smooth results are shown together with the observations for each of the four measured  
 810 channels (heights).





811

812 Figure 6. Standard deviation of the EMI series (horizontal black line) for the 50-6dS transect at  
 813 0.2-0.4 m depth. The squares show the corresponding standard deviations for the TDR series  
 814 for different level of filtering. The intersection of the EMI line with the TDR curve allows  
 815 identifying the optimal cut-off frequency range (~0.313 cycles/m) to make the two standard  
 816 deviations similar.

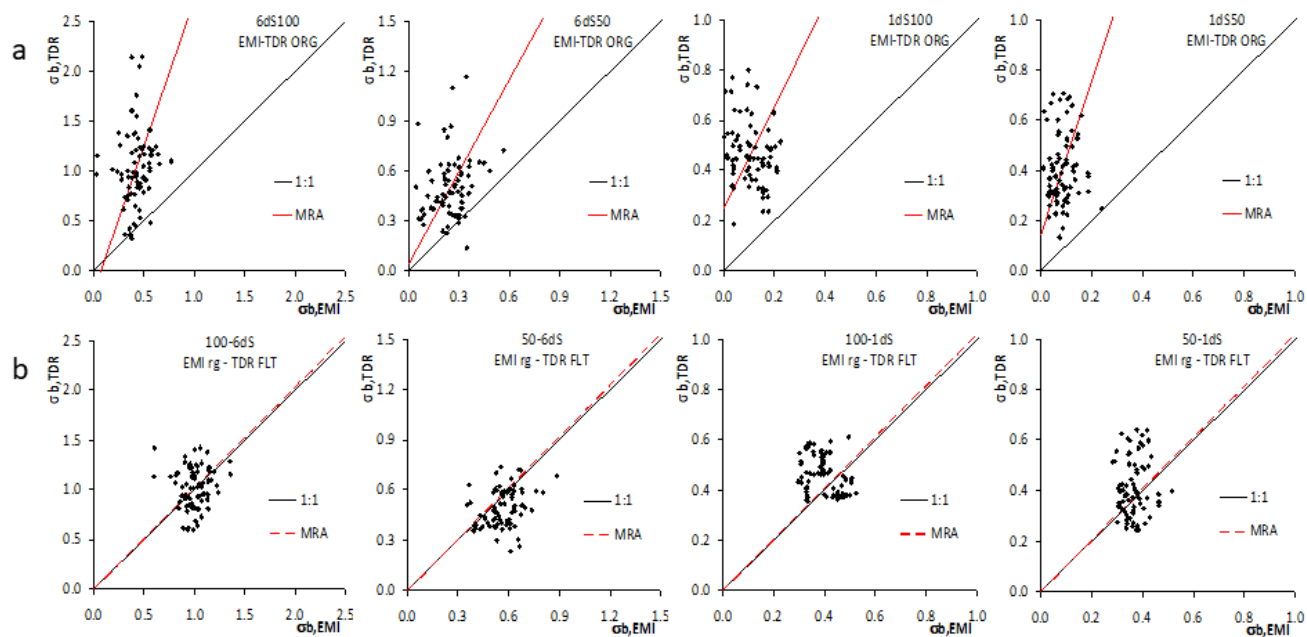


Figure 7. Comparison between  $\sigma_{b,TDR}$  and  $\sigma_{b,EMI}$  for all four transects for the depth range 0.0-0.6 m. The graphs in the top panels (a) show the original TDR and EMI data, while those in the bottom panels (b) the Filtered (FLT) TDR and EMI data after the regression based on MRA parameters (rg).

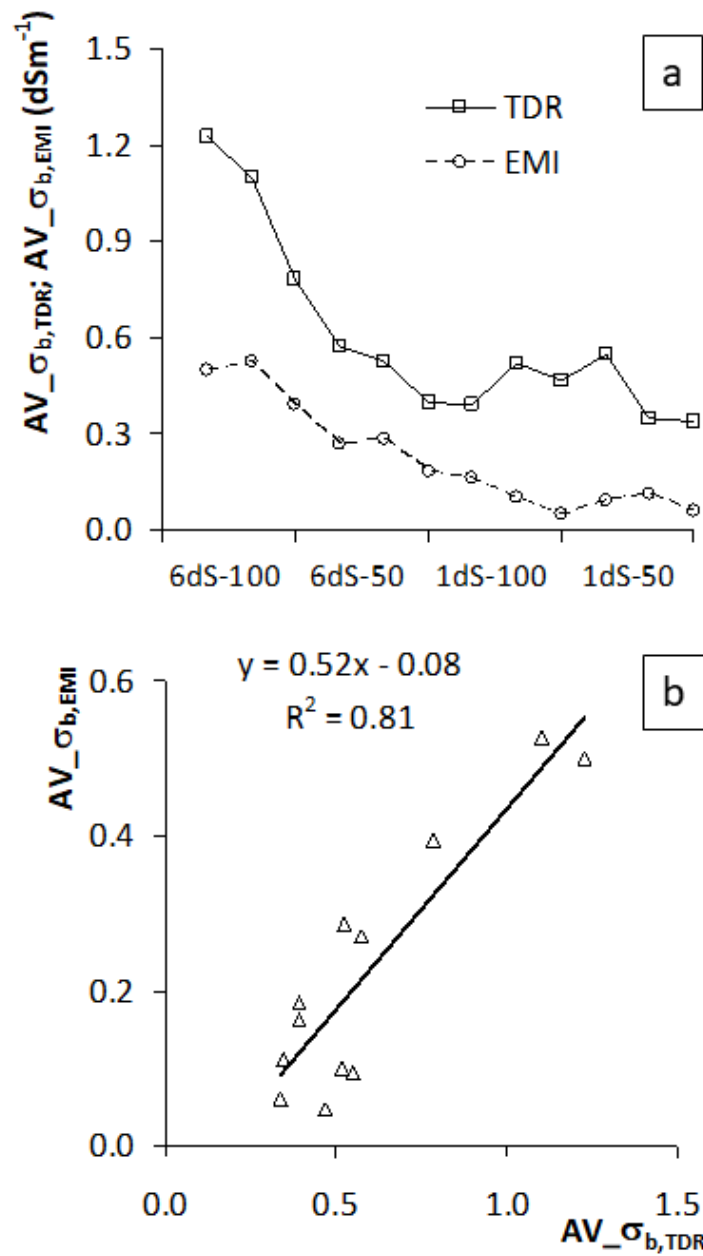


Figure 8. (a) Comparison of the means for the two original series (squares-solid line for TDR, dcircles-dashed line for EMI); (b) The same comparison on a 1:1 plot (triangles-solid regression line). In the panel (a), the four cases are shown in sequence. For each case, the three values are for the three depth intervals 0.0-0.2, 0.2-0.4, and 0.4-0.6 m.

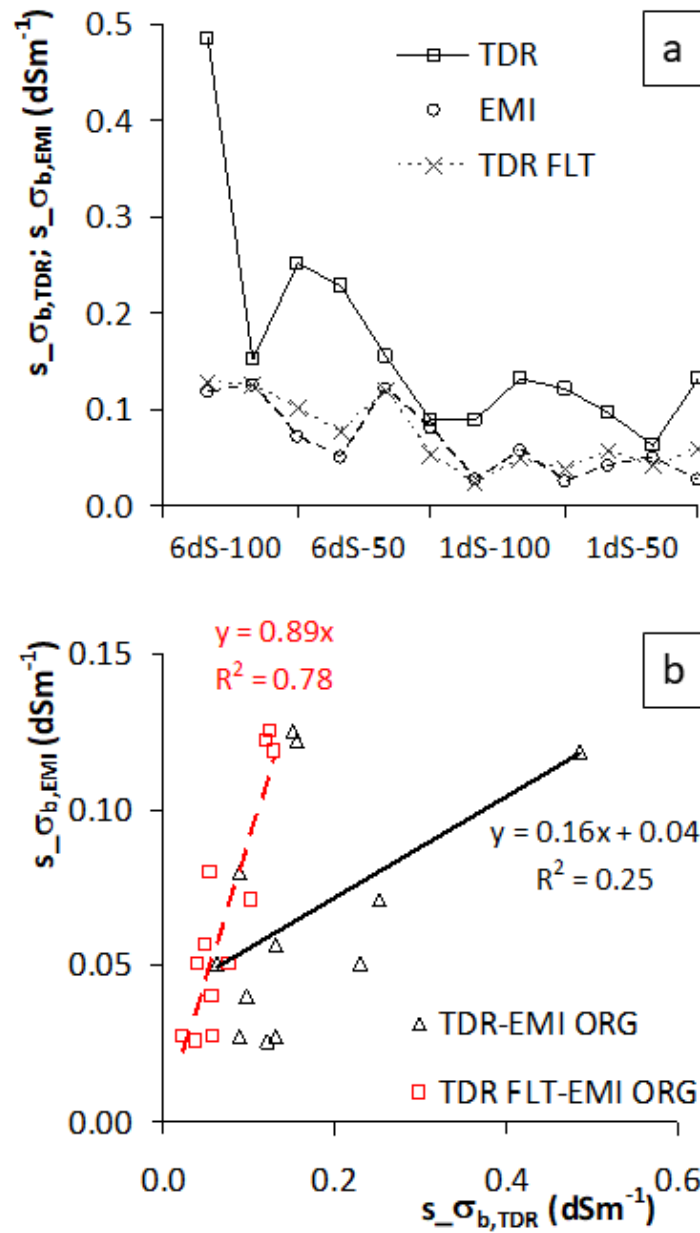


Figure 9. (a) Comparison of the standard deviations of the TDR original series (squares-solid line), of the EMI original series (circles-dashed line), and of the filtered (FLT) TDR series (crosses-dashed line); (b) The same comparison on a 1:1 plot: the original TDR and EMI data (triangles-solid regression line); filtered (FLT) TDR and original EMI data (squares-dashed regression line). In the panel (a), the four cases are shown in sequence. For each case, the three values are for the three depth intervals 0.0-0.2, 0.2-0.4, and 0.4-0.6 m.

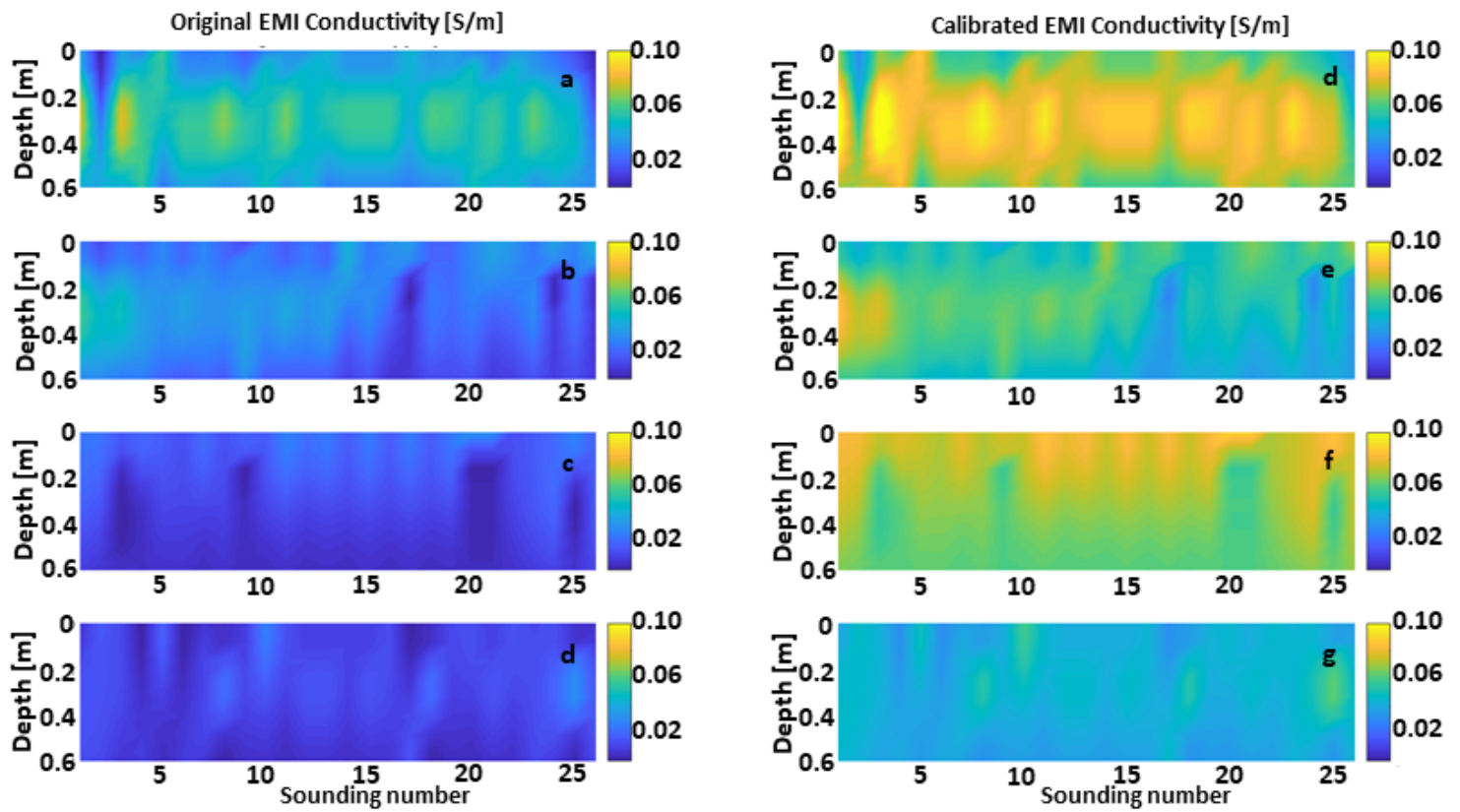


Figure 10. Maps of bulk electrical conductivity for the: (a) 100-6dS, (b) 50-6dS, (c) 100-1dS, (d) 50-1dS transects showing the original  $\sigma_{b,EMI}$  resulting from the inversion of the observed EMI data. Panels (d) to (g) show instead the corresponding results after the calibration via the TDR measurements (i.e., by applying Eq. 10).

<b>Transect</b>	<b>C<sub>b</sub></b>	<b>ρ<sub>L</sub></b>	<b>ρ<sub>P</sub></b>	<b>β</b>	<b>α</b>
<b>100-1dS</b>	0.10	0.02	0.33	2.04	0.25
<b>50-1dS</b>	0.10	0.00	0.08	3.06	0.14
<b>100-6dS</b>	0.18	0.02	0.07	2.92	-0.21
<b>50-6dS</b>	0.34	0.08	0.32	1.84	0.04

Table 1. Concordance parameters for the four transects for the TDR\_ORG and EMI\_ORG data. The table reports the Concordance,  $\rho_L$ , and the Pearson,  $\rho_P$ , correlation, as well as parameters  $\alpha$  and  $\beta$  of the MRA line. The bias factor,  $C_b$ , is also shown.

<b>Transect</b>	<b>C<sub>b</sub></b>	<b>ρ<sub>L</sub></b>	<b>ρ<sub>P</sub></b>	<b>β</b>	<b>α</b>
<b>100-1dS</b>	0.74	0.24	0.33	1.02	0.29
<b>50-1dS</b>	0.62	0.05	0.08	1.02	0.27
<b>100-6dS</b>	0.87	0.06	0.07	1.02	0.57
<b>50-6dS</b>	0.79	0.25	0.32	1.02	0.31

Table 2. Concordance parameters for the four transects for the TDR\_FLT and EMI\_ORG data. The table reports the Concordance,  $\rho_L$ , and the Pearson,  $\rho_P$ , correlation, as well as parameters  $\alpha$  and  $\beta$  of the MRA line. The bias factor,  $C_b$ , is also shown.